Published in final edited form as:
Biomaterials. 2013 April ; 34(12): 2980–2990. doi:10.1016/j.biomaterials.2013.01.046.

Pegylated siRNA-loaded calcium phosphate nanoparticle-driven amplification of cancer cell internalization *in vivo*

Lisa A. Tobin[a], **Yili Xie**[a], **Maria Tsokos**[b,c,d], **Su I. Chung**[a], **Allison A. Merz**[a], **Michael A. Arnold**[b,e], **Guang Li**[b], **Harry L. Malech**[f], and **King F. Kwong**[a,g,*]

[a]Thoracic Oncology Section, Surgery Branch, National Cancer Institute, National Institutes of Health, Bethesda, MD, USA

[b]Laboratory of Pathology, National Cancer Institute, National Institutes of Health, Bethesda, MD, USA

[c]Department of Medicine, Beth Israel Deaconess Medical Center, Harvard University Medical School, Boston, MA, USA

[d]Department of Pathology, Beth Israel Deaconess Medical Center, Harvard University Medical School, Boston, MA, USA

[e]Department of Pathology and Laboratory Medicine, Nationwide Children's Hospital, Columbus, OH, USA

[f]Laboratory of Host Defenses, National Institute of Allergy and Infectious Diseases, National Institutes of Health, Bethesda, MD, USA

[g]Center for Cancer Research, National Cancer Institute, National Institutes of Health, Bethesda, MD, USA

Abstract

The cell membrane is a critical barrier to effective delivery for many therapeutics, including those which are nanoparticle-based. Improving nanoparticle transport across the cell membrane remains a fundamental challenge. Cancer cells preferentially internalized pegylated calcium phosphate nanoparticles over normal epithelial cells. Furthermore, non-cytotoxic levels of doxorubicin markedly amplified this difference by increasing free unbound caveolin-1 and resulted in enhanced caveolin-mediated nanoparticle endocytosis in cancer cells. Engineered pegylated siRNA-loaded triple-shell calcium phosphate nanoconstructs incorporating ultra-low levels of doxorubicin recapitulated these effects and delivered increased numbers of siRNA into cancer cells with target-specific results. Systemic administration of nanoparticles *in vivo* demonstrated highly preferential entry into tumors, little bystander organ biodistribution, and significant tumor growth arrest. In conclusion, siRNA-loaded calcium phosphate nanoparticles incorporating non-cytotoxic amounts of doxorubicin markedly enhances nanoparticle internalization and results in increased payload delivery with concomitant on-target effects.

Keywords

Nanoparticle; Calcium phosphate; *In vivo* delivery; Endocytosis; Cancer; siRNA

[*]Corresponding author. National Cancer Institute, National Institutes of Health, 10 Center Drive, MSC 1201, Bethesda, MD 20892-1201, USA. Tel.: +1 301 435 7504. kwongk2@mail.nih.gov. .

Appendix A. Supplementary data Supplementary data related to this article can be found at http://dx.doi.org/10.1016/j.biomaterials.2013.01.046.

1. Introduction

The unique physical properties of nanoparticles (size, shape, composition, and charge) can result in preferential localization in both the tumor vasculature and tumor interstitium via the enhanced permeability and retention (EPR) effect [1] found selectively in tumors due to extensive neo-angiogenesis required for tumor establishment, maintenance, and growth. The increased permeability found in the tumor vasculature, manifested chiefly by the loss of tight endothelial junctions [2], allows for vascular extravasation of nanoconstructs of varying sizes selectively into the tumor micro-environment [3]. Facilitated transport across the cell membrane via endocytosis is thought to play an important role in nanoparticle cell-entry; however, until now this process has not been targeted for augmentation. Clathrin- and caveolin-mediated endocytosis represents two distinct mechanisms of cellular entry. Notably, caveolin-mediated endocytosis has been reported to participate in the internalization of nanoparticles such as polylactic acid polymeric micelles [4], cyclodextrin polyplexes [5], polystyrene [6], and mesoporous silica [7]. Historical electron microscopy data suggested engagement of specific endocytosis pathways are restricted by particle size, but more recent data suggests that nanoparticles ranging from as small as 45 nm to those as large as 300 nm can enter cells via caveolin-dependent processes [4,7]. Alternatively, targeting approaches involving RGD peptide [8] or folate receptors [9] may also utilize the endocytosis pathway for cell-entry but do not alter the intrinsic endocytic capacity of the cancer cell. To our knowledge, nanoconstructs which specifically enhance nanoparticle endocytosis have not been reported.

There is significant ongoing interest to deliver siRNAs and therapeutic drugs to tumors via nanoparticles; however, limited nanoparticle cell-entry has remained a major challenge to advancing the field. In early work, the use of therapeutic siRNAs was hampered by several hurdles including siRNA degradation in the bloodstream by plasma nucleases and sequestration of unprotected siRNA nanoparticles by the body's reticulo-endothelial system, thus limiting systemic siRNA delivery essentially only to the liver and spleen [10]. To date, siRNA has been incorporated into lipid-based [11–13], atelocollagen [14], and polyethyleneimine [15] particles for *in vivo* gene silencing, but efficient transfer across the cell membrane, favorable blood half-life, and adequate tissue bioavailability [16] remain significant challenges.

In this report, we studied the endocytosis of pegylated triple-shell calcium phosphate nanoparticles in cancer cells in order to improve nanoparticle internalization. We hypothesized that improved cellular internalization of nanoparticles would lead to improved payload delivery and consequently augment therapeutic effects. Our approach began with a quantitative analysis using fluorescence confocal microscopy to detect internalized intracellular nanoparticles and to delineate the relative contributions of the two main endocytosis pathways in the cellular uptake of pegylated triple-shell calcium phosphate nanoparticles. These data ultimately led to the engineering of a nanoparticle incorporating an endocytosis-enhancing component, which we evaluated for their siRNA-delivery capability in both *in vitro* and *in vivo* experiments.

2. Materials and methods

2.1. Reagents

$CaCl_2$, Na_2HPO_4, 4-(Dimethylamino)pyridine (DMAP), N-(3-Dimethylaminopropyl)-N'-ethylcarbodiimide hydrochloride (EDC), *O,O'*-Bis(2-aminopropyl) polypropylene glycol-*block*-polyethylene glycol-*block*-polypropylene glycol 1900 (PEG), NaOH, and 3-(4,5-Dimethyl-2-thiazolyl)-2,5-diphenyl-2H-tetrazolium bromide (MTT) were purchased from Sigma (St. Louis, MO). siRNA negative control, siRNA against XIAP (5′-

CATGCAGCTGTAGATAGATGGCA-3′) [17], PARP1 (5′-AAGCCTCCGCTCCTGAACAAT-3′) [18], VEGF (5′-CGATGAAGCCCTGGAGTGC-3′)[15,17], and EGFR (5′-AACACAGTGGAGCGAATTCCT-3′) [19,20] were purchased from Thermo Scientific/Dharmacon (Lafayette, CO). DyLight 550 NHS Ester, DyLight 755 NHS Ester, DyLight 488 Antibody Labeling Kit and DyLight 633 Antibody Labeling Kit were purchased from Thermo Scientific/Pierce (Rockford, IL). Chlorpromazine (CPZ), genistein (GEN), paclitaxel, doxorubicin (DOX), and etoposide were purchased from Sigma.

2.2. Preparation of triple-shell calcium phosphate nanoparticles containing doxorubicin and siRNA

Triple-shell calcium phosphate nanoparticles were prepared by a modified precipitation method as previously described [21,22]. The primary calcium phosphate core or "single-shell" was self assembled by adding Na_2HPO_4 (3.74 mM) and DyLight 550 or 755 (2 μg/mL) incrementally to $CaCl_2$ (6.25 mM) and siRNA (6.25 μg/mL) with agitation. To obtain "double-shell" particles, $CaCl_2$ (6.25 mM) and doxorubicin (20 ng/mL) and Na_2HPO_4 (3.74 mM) and DyLight 550 or 755 (2 μg/mL) were then added to the "single-shell" nanoparticles. To obtain "triple-shell" particles, $CaCl_2$ (6.25 mM) and Na_2HPO_4 (3.74 mM) were added to the "double-shell" nanoparticles. The resulting triple-shell nanoparticles were filtered through an Amicon Ultra-15 centrifugal filter unit with an Ultracel-100 membrane (Millipore) and washed twice with 4-(Dimethylamino)pyridine (DMAP; 1 mg/mL). The nanoparticles were then incubated in DMAP (1 mg/mL) and N-(3-Dimethylaminopropyl)-N'-ethylcarbodiimide hydrochloride (EDC; 25 mg/mL) at 4 °C for 45 min under constant rotation. The nanoparticles were then washed twice in PBS and resuspended in a 25 mg/mL solution of *O,O'*-Bis(2-aminopropyl) polypropylene glycol-*block*-polyethylene glycol-*block*-polypropylene glycol 1900 (PEG; Sigma) for 16 h at 4 °C under constant rotation. Then, nanoparticles were filtered through a 0.45 μm Millex HA filter unit (Millipore) followed by an Amicon Ultra-15 centrifugal filter unit with an Ultracel-100 membrane, washed twice with PBS, and stored at 4 °C until use.

2.3. Nanoparticle characterization

Nanoparticle size distribution was measured by dynamic light scattering using a DynaPro Nanostar machine (Wyatt Technology Corporation, Santa Barbara, CA) or Malvern ZetaSizer Nano ZS with backscattering detector (Malvern Instruments Inc., Westborough, MA). Zeta potential was measured in 10 mM NaCl at pH 7.1 using a Malvern Zetasizer Nano ZS. To measure incorporation, nanoparticles were disassociated using HCl and then siRNA and doxorubicin were measured spectrophotometrically at 230 nm and 479 nm, respectively, using the Nanodrop ND-1000 spectro-photometer (Thermo Scientific, Wilmington, DE). DyLight 550 or 755 was measured at 560 or 750 nm, respectively, using a Nanodrop spectrophotometer. Nanoparticle stability was characterized by incubating the nanoparticles in a range of pH (0.1–10.1) or temperature (4–42 °C) and then RNA concentration was measured using a Nanodrop spectro-photometer.

2.4. Cells

Human small airway epithelial cells (SAEC) and human mammary epithelial cells (HMEC) were purchased from Lonza (Walkersville, MD). A549, H520, H292, and SKLU-1 non-small cell lung cancer (NSCLC) cell lines, MDA-MB-231 breast cancer cells, PC3 prostate cancer cells, and HeLa cervical cancer cells were purchased from ATCC (Manassas, VA). OE21 esophageal cancer cells were purchased from Sigma (St. Louis, MO). SAEC cells were grown in small airway epithelial basal medium (Lonza) supplemented with BPE, hydrocortisone, hEGF, epinephrine, insulin, triiodothyronine, transferrin, gentamicin/amphotericin-B, retinoic acid and BSA-FAF (Lonza SAGM SingleQuots). HMEC cells

were maintained in mammary epithelial basal medium (Lonza) supplemented with BPE, hydrocortisone, hEGF, insulin and gentamicin/amphotericin-B (Lonza MEGM SingleQuots). A549 and PC3 were grown in F-12 medium (Gibco, Carlsbad, CA). H520, H292, and OE21 were grown in RPMI 1640 medium (Gibco). MDA-MB-231 cells were grown in DMEM high glucose medium (Gibco). SKLU-1 and HeLa cells were maintained in MEM medium (Mediatech, Manassas, VA). All media were supplemented with 10% FBS and cells were maintained at 37 °C in a 5% CO_2 humidified atmosphere.

2.5. Fluorescence confocal microscopy

5×10^3 cells were plated onto 8-well u-slides (ibidi, Martinsried, Germany) for 24 h prior to use and incubated under routine conditions (described above). Equal numbers of nanoparticles were applied to each culture well and time-elapsed confocal microscopy was performed using the Zeiss LSM 710 system (Zeiss North America, New York, NY). Anti-(free) caveolin-1 (BD Biosciences) and anti-clathrin HC (Santa Cruz) antibodies were labeled with DyLight 633 or DyLight 488 Antibody Labeling Kits (Thermo Scientific/Pierce), respectively, according to the manufacturer's protocol. Intracellular fluorescent intensities compiled from five z-stacks were analyzed using ZEN 2009 (Zeiss), Zeiss LSM Image Browser (Zeiss), and ImageJ software.

2.6. RNA isolation and quantitative real-time RT-PCR

H292 cells were incubated with NPs (NP-siRNA-Dy550, NP-DOX-Dy550 or NP-DOX-siRNA-Dy550) for 24 h. Total RNA was isolated from cultured cells according to the manufacturer's protocol (Qiagen RNeasy Mini Kit and QIAshredder). TaqMan Gene Expression Assays (Life Technologies/Applied Biosystems) for XIAP (Hs00745222_s1), PARP (Hs00242302_m1), VEGF (Hs00900055_m1), EGFR (Hs01076078_m1), CAV1 (Hs00971716_m1), and GAPDH (Hs02758991_g1) were used to perform quantitative real-time RT-PCR on 100 ng of total RNA in a 20 μL reaction volume with TaqMan® RNA-to-CT™ 1-Step Kit (Life Technologies/Applied Biosystems) in an Applied Biosystems StepOnePlus Real-Time PCR System according to the manufacturer's protocol. The expression levels of XIAP, PARP, VEGF, EGFR, and CAV1 were normalized to that of GAPDH.

2.7. Reactive oxygen species

H292 cells were incubated with NP-DOX-siXIAP-Dy550 for up to 1 h. SAEC cells were incubated with doxorubicin for up to 1 h. The cells were collected and washed with PBS prior to 45 min incubation with dihydroethidium (Life Technologies) at 37 °C. Cells were washed twice with PBS and flow cytometry was performed using a BD Biosciences FACSCanto II flow cytometer and analyzed with FlowJo software (TreeStar).

2.8. Immunoblotting

Cells were washed twice with PBS, and lysed using 1× RIPA lysis buffer (Millipore, Temecula, CA) (50 mM Tris–HCl, 150 mM NaCl, 1% NP-40, 0.5% sodium deoxycholate, 2 mM sodium fluoride, 2 mM EDTA, 0.1% SDS) and 1× protease inhibitor (Crystalgen, Inc., Commack, NY). Tumor tissues were harvested from animals and immediately snap-frozen in liquid nitrogen. Thawed tumor tissues were mechanically homogenized in cold homogenization buffer (20 mM tris (hydroxymethyl) aminomethane hydrochloride (Tris-HC1), 1 mM ethylene glycol-bis(/3-aminoethylether)-N,N,N',N'-tetraacetic acid (EGTA), 5 mM sodium azide, 50 mM sodium chloride, 10 mM/3-mercaptoethanol, phenylmethylsulfonyl 2 mM fluoride, pH 7.4) with 1× RIPA lysis buffer (Millipore) and 1× protease inhibitor (Crystalgen, Inc.) and then centrifuged at 12,000 rpm for 10 min at 4 °C to obtain the supernatant fraction. Cell or tissue cell lysates, containing equal amounts of protein, were

mixed with SDS protein gel loading solution, resolved in SDS-PAGE gel and transferred to nitrocellulose membranes. The membranes were blocked in 3% non-fat milk in PBS with 0.1% Tween 20, pH 7.6 for 30 min then incubated with the appropriate primary antibodies (1:1000–1:5000) at 4 °C overnight: anti-XIAP (BD Biosciences, San Diego, CA, USA), anti-PARP (Cell Signaling, Danvers, MA), anti-EGFR (Cell Signaling), anti-VEGF (Santa Cruz), anti-caveolin-1 (BD Biosciences), anti-eNOS/NOS Type III (BD Biosciences), and GAPDH (BD Biosciences). Then, membranes were incubated in either goat anti-rabbit or anti-mouse secondary antibodies (1:2000) for 1 h at room temperature. Membranes were then exposed to Supersignal West Femto Substrate (Pierce, Rockford, IL, USA) and visualized using an EC3 imaging system (UVP, Upland, CA). Densitometry was performed using ImageJ software.

2.9. Cell viability assay

Cells were seeded in 24-well plates at predetermined plating densities appropriate for each cell line (1–2 × 10^5 cells/well) 24 h prior to use. Then, cells were treated with triple-shell calcium phosphate doxorubicin-siRNA nanoparticles (NP-DOX-siRNA-Dy550; 30 pmol siRNA and 50 nM DOX), DOX nanoparticles (NP-DOX-Dy550; 50 nM), siRNA nanoparticles (NP-siRNA-Dy550; 30 pmol siRNA) or siRNA negative control nanoparticles (NP-siCTRL-Dy550; 30 pmol) for 48 h. Cell viability was determined by 3-(4,5-Dimethyl-2-thiazolyl)-2,5-diphenyl-2H-tetrazolium bromide (MTT) assay and expressed as a percentage of viable cells relative to untreated cells.

2.10. In vivo nanoparticles targeting XIAP

All *in vivo* procedures were conducted in compliance with the Guide for the Care and Use of Laboratory Animal Resources (1996), US National Research Council, and approved by the National Cancer Institute/NIH Animal Care and Use Committee. Four to six week-old female homozygote athymic nude mice were purchased from Charles River (National Cancer Institute, Frederick, MD). Three million H292 cells were resuspended in 50 μL of RPMI 1640 (Gibco) and 50 μL of matrigel (BD Biosciences) and injected subcutaneously into the right flank of each mouse. Palpable subcutaneous tumors were measured twice-weekly using digital calipers and tumor volume was calculated by the formula, tumor volume = 0.5 × length × width × height [23]. When tumor volume reached 40–70 mm^3, the mice were randomized and received either triple-shell calcium phosphate nanoparticles with doxorubicin (DOX) and siRNA against XIAP (siXIAP) (NP-DOX-siXIAP-Dy755), NPs with DOX and without siXIAP (NP-DOX-Dy755) or nanoparticles with siXIAP and without doxorubicin (NP-siXIAP-Dy755), administered via tail vein injections twice-weekly for 6 total injections or were left untreated. During imaging, mice were anesthesized with isoflurane. Near-infrared (NIR) imaging was performed at each time point with a Pearl Imager (LI-COR Biosciences, Lincoln, NE) using a 700-nm fluorescence channel.

2.11. Biodistribution analysis

Nanoparticle biodistribution studies utilized the H292 xenograft model and consisted of a single tail-vein injection with triple-shell calcium phosphate doxorubicin-siXIAP nanoparticles at the same nanoparticle dose used in treatment experiments and animals were then euthanized at 48, 72, and 96 h. Mice treated with twice-weekly NP injections were euthanized at day 22 following a total of 6 doses. At euthanasia, all tissue organs were harvested and snap-frozen in liquid nitrogen for subsequent analysis. Tissues were then homogenized in cold homogenization buffer (described above) and then centrifuged at 14,000 rpm for 15 min at 4 °C to obtain the supernatant fraction. 2 μL HCl (11.6 M, Sigma) was added to 10 μL of the tissue-derived supernatant and then analyzed at 740 nm using the Nanodrop ND-1000 spectrophotometer.

2.12. Histochemistry and electron microscopy

Control and treated animals underwent tumor excision and organ harvest at time of euthanasia. All tissues were snap-frozen in liquid nitrogen and small portions were preserved in 4% paraformaldehyde in PBS (USB Corporation, Cleveland, OH). Immunohistochemical staining was performed on paraformaldehyde-fixed paraffin-embedded (PFPE) tissues. Antigen retrieval was performed by heating the slides in antigen retrieval solution, pH 6.0 (DAKO Corporation, Carpinteria, CA) for 20 min. Endogenous peroxidase activity and non-specific signal were blocked by incubation with peroxidase block and protein block serum-free solutions. Subsequently, the sections were stained at room temperature with mouse anti-XIAP antibody (BD Biosciences, San Jose, CA) for 2 h at 1:25 dilution, followed by anti-mouse secondary antibody (EnVision-Plus HRP reagent, DAKO) for 30 min. The reaction was developed with diaminobenzidine (DAB) chromogen (DAKO) and the slides were counterstained with hematoxylin.

Mouse cardiac tissues submitted to ultrastructural examination were fixed in PBS-buffered glutaraldehyde (2.5%), postfixed in osmium tetroxide (0.5%), dehydrated and embedded in Spurr's epoxy resin. Ultrathin sections were stained with uranyl acetate and lead citrate and viewed in a Philips CM10 transmission electron microscope. Immuno-EM was performed on cells pelleted in 1.5% low melting point agarose, washed with PBS (3×, 5 min), dehydrated in ethanol series, and embedded in LR White (SPI, West Chester, PA). Ultrathin sections (~90 nm) were mounted on 150-mesh uncoated nickel grids. Grids were floated on blocking solution (PBS, 0.1% Tween 20, 0.5% cold-water fish gelatin, Ted Pella, Inc., Redding, CA) for 20 min, incubated for 1 h with primary antibody (anti-caveolin-1, BD Biosciences), rinsed three times in blocking buffer, and floated on 20 nm gold-conjugated Protein-A (Ted Pella, Inc., Redding, CA), rinsed in PBS, water, and air dried. Sections were stained with aqueous uranyl acetate and examined with Phillips CM10 and JEOL JEM1010 electron microscopes.

2.13. Statistical analyses

Statistical evaluation for data analysis was determined using paired Student's *t*-test and repeated-measures ANOVA. All data were shown as the mean ± s.e.m. Statistical difference was assigned to $p < 0.05$.

3. Results

3.1. Intrinsic calcium phosphate nanoparticle cell-entry

To evaluate the baseline uptake of pegylated triple-shell calcium phosphate nanoparticles labeled with DyLight 550 fluorescent dye (NP-Dy550), we measured time-dependent accumulation of fluorescence in a panel of normal epithelial (SAEC and HMEC) and cancer (A549, H292, H520, SKLU-1, MDA-MB-231, PC3, HeLa, and OE21) cells over a 4 h period by fluorescence confocal microscopy. NP-Dy550 was detected in cancer cells within 10 min after administration with maximal fluorescence seen at 4 h (Fig. 1a). Intrinsic nanoparticle accumulation varied among the cancer cells tested with A549 exhibiting the greatest nanoparticle relative fluorescence while SKLU-1 and PC3 had more limited nanoparticle entry. Non-cancer cells such as normal small airway (SAEC) and human mammary (HMEC) treated under identical conditions, exhibited negligible nanoparticle uptake (Fig. 1a).

3.2. Nanoparticle endocytosis

Calcium phosphate nanoparticles, like other types of NPs, have been reported to enter cells via endocytosis [24]; however, the extent to which clathrin- and/or caveolin-endocytosis may facilitate NP cell-entry is not well defined. Accordingly, we first determined baseline

clathrin and free (unbound) caveolin-1 expression in A549, H292, H520, and MDA-MB-231 cancer cells (Fig. 1b), and subsequently pre-treated the cells with either chlorpromazine (CPZ), an inhibitor of clathrin-mediated endocytosis [25], or genistein (GEN), an inhibitor of caveolin-mediated endocytosis [25], prior to a 0.5 h incubation with NP-Dy550 nanoparticles. CPZ pre-treatment did not alter the number of nanoparticles entering cancer cells, suggesting minimal contribution of clathrin-mediated endocytosis (Fig. 1c). Conversely, GEN pre-treatment significantly inhibited nanoparticle entry in all cancer cell lines tested (Fig. 1c). Taken together, these data suggest that caveolin-mediated endocytosis is a primary mechanism facilitating calcium phosphate nanoparticle entry into cancer cells for a variety of cancer histiotypes.

3.3. Caveolin-mediated nanoparticle uptake in cancer cells

Doxorubicin (DOX), paclitaxel, and etoposide have been associated with increased caveolin-1 expression in cancer cells [26]. Together with our observation that caveolin-mediated endocytosis is a primary mechanism for calcium phosphate nanoparticle entry into cancer cells, we hypothesized that increasing caveolin-1 via these chemotherapeutics would lead to increased nanoparticle uptake. To test this hypothesis, we pre-treated normal and cancer cells with non-cytotoxic levels of doxorubicin, paclitaxel, or etoposide for 2 h followed by a 0.5 or 4 h incubation with NP-Dy550 nanoparticles. After doxorubicin pre-treatment and a 0.5 h NP-Dy550 incubation, intracellular caveolin-1 levels increased from 2.5 to 10.5-fold and intracellular nanoparticle numbers rose from 2.3 to 64.5-fold in all cancer cell lines compared to controls in confocal immunofluorescence studies (Supplemental Fig. 1). Following doxorubicin pre-treatment and a longer 4 h incubation with NP-Dy550, both caveolin-1 levels and intracellular nanoparticle numbers rose even higher, up to a 25.7-fold increase in caveolin-1 fluorescence and up to a 132.3-fold increase in intracellular NP-Dy550 in cancer cells compared to controls (Fig. 1d–g). In SAEC and HMEC non-cancer epithelial cells, caveolin-1 expression remained relatively unchanged despite pre-treatment with DOX and resistance to nanoparticle uptake persisted even after a 4 h incubation with NP-Dy550 nanoparticles (Fig. 1d–e). Similar pretreatment with non-cytotoxic levels of paclitaxel or etoposide also resulted in increased caveolin-1 fluorescence and intracellular NP-Dy550 (Supplemental Fig. 1); however, doxorubicin pre-treatment resulted in the highest increases in caveolin-1 and NP-Dy550 intracellular fluorescence overall.

3.4. Triple-shell calcium phosphate nanoparticles with doxorubicin and siRNA

In order to take advantage of amplified nanoparticle entry in cancer cells by doxorubicin while avoiding systemic exposure, we generated a pegylated triple-shell calcium phosphate nanoparticle with ultra-low amounts of doxorubicin incorporated into the secondary (middle) shell (NP-DOX-Dy550). We also engineered pegylated triple-shell calcium phosphate nanoparticles with therapeutic siRNA within the centrally-located primary shell and DOX in the secondary shell to form NP-DOX-siRNA-Dy550 (Fig. 2a). Nanoparticles with non-specific negative control siRNA (siCTRL) or siRNA against XIAP (NP-siCTRL-Dy550 and NP-siXIAP-Dy550, respectively) served as controls. NP-siCTRL-Dy550, NP-DOX-Dy550, NP-siXIAP-Dy550, and NP-DOX-siXIAP-Dy550 measured 154–157 nm in diameter by dynamic light scattering (Fig. 2b) with NP-DOX-siRNA-Dy550 having a zeta potential of -8.8 ± 1.4 mV at pH 7.1. Pegylated single, double, and triple-shell nanoparticles labeled with DyLight 550 measured 73, 109, and 127 nm in diameter, respectively, suggesting the addition of additional shells during synthesis (Fig. 2b).

In order to test the stability of NP-DOX-siXIAP-Dy550, we measured the release of siRNA over a range of pH and temperatures. The particles remained stable in pH 4 to 10 for up to

45 min (Fig. 2c). NP-DOX-siXIAP-Dy550 was also stable from 4 to 42 °C for up to 45 min (Fig. 2d).

3.5. Endocytosis of doxorubicin-incorporated nanoparticles

We hypothesized that DOX-incorporated nanoconstructs would lead to compounding increases in NP internalization in cancer cells through enhanced caveolin-mediated endocytosis. H292 cells were incubated with nanoparticles containing siRNA negative control (NP-siCTRL-Dy550) or NP-DOX-Dy550 for a 0.5 or 4 h period. After 0.5 h, both caveolin-1 levels and the number of internalized nanoparticles were significantly higher in cells treated with NP-DOX-Dy550 (Fig. 3a). After a 4 h incubation with NP-DOX-Dy550, a 9-fold increase in both caveolin-1 and NP-DOX-Dy550 internalization was observed compared to NP-siCTRL-Dy550 treatment (Fig. 3a–b). Increases in caveolin-1 levels in H292 cells were also confirmed by immunogold electron microscopy after 4 h incubation with nanoparticles containing DOX and siRNA against XIAP, NP-DOX-siXIAP-Dy550 (Fig. 3c).

Doxorubicin has been reported to increase intracellular reactive oxygen species and to disassociate endothelial nitric-oxide synthase (eNOS)-caveolin complexes to rapidly expand the intracellular pool of free caveolin-1 [27]. In support of this mechanism, we measured caveolin-1 mRNA levels in H292 cancer cells 24 h after administration of NP-DOX-siRNA-Dy550 with siRNA against XIAP, PARP, VEGF or EGFR using real-time PCR. No changes in caveolin-1 mRNA transcripts were found despite increases in intracellular reactive oxygen species and free caveolin-1 protein levels in as little as 1 h after NP treatment (Fig. 4a–c), suggesting that the increase in free caveolin-1 protein is not due to increased mRNA expression. Importantly, doxorubicin treatment in SAEC normal epithelial cells, which exhibit negligible NP uptake, did not alter reactive oxygen or caveolin-1 levels (Fig. 4d–e).

3.6. Biological effects of NP-DOX-siRNA-Dy550 in vitro

To assess the versatility and specificity of delivering different siRNAs with doxorubicin-incorporated nanoconstructs, we treated H292 cells with NP-DOX-siRNA-Dy550 nanoparticles containing siRNAs specific for XIAP, PARP, VEGF or EGFR, which are important mediators of cancer cell survival. Consequently, treated H292 cells exhibited marked specific attenuation of XIAP, PARP, VEGF or EGFR mRNAs following treatment with the corresponding DOX-incorporated nanoparticles compared to controls (Fig. 5a). A *bona fide* nano-effect of the calcium phosphate nanoconstructs was further confirmed by the lack of detectable XIAP knockdown following treatment of H292 cells with the individual or collective unassembled components of NP-DOX-siXIAP-Dy550 (Fig. 5b). Enhanced nanoparticle entry due to doxorubicin incorporation resulted in both decreased target protein levels (Fig. 5c–f) and significant reductions in cellular viability (Fig. 5g–j) compared to controls. NPs containing siRNA without doxorubicin (i.e. NP-siRNA-Dy550) resulted in only minimal attenuation of protein expression (Fig. 5c–f), and correspondingly smaller losses in cell viability were seen compared to NP-DOX-siXIAP-Dy550 (Fig. 5g–j). These data suggest that DOX incorporation into NPs results in enhanced nanoparticle uptake in cancer cells, increased siRNA delivery, and greater knockdown of target proteins.

3.7. In vivo trafficking of multi-shell nanoparticles

To determine the anatomic distribution of intravenously administered nanoparticles, we measured the amount of DyLight 755 (Dy755) fluorescence retrieved from distinct anatomic organs after the administration of a single intravenous dose of NP-DOX-siXIAP-Dy755 nanoparticles in H292 tumor-bearing mice (Fig. 6a). At 48 h after nanoparticle injection, kidney and intestinal localization of nanoparticles predominated, representing renal clearance and normal physiologic calcium processing by the intestinal tract. Evidence that

the intestinal tract participates in the clearance of calcium-based nanoparticles was also demonstrated by detectable DyLight 755 signal in mouse fecal matter; therefore, the intestinal NP signal seen in the early period likely represents transient trafficking through the intestinal tract and not true tissue accumulation. Renal localization of nanoparticles was dramatically diminished by 72 h, representing complete clearance of the administered nanoparticle dose from the systemic circulation. At 72 h and subsequently thereafter, marked accumulation of nanoparticles was seen principally in the tumor, where it retained the highest levels of nanoparticles of all anatomic sites.

We also examined the biodistribution of twice-weekly intravenous injections of NP-DOX-siXIAP-Dy755 in H292 tumor-bearing mice for a period of 22 days (Fig. 6b). The anatomic biodistribution profile of these mice also showed preferential tumor accumulation of NPs and at levels higher than with a single dose. No significant accumulation of nanoparticles in the heart or other bystander organs was evident.

3.8. Multi-shell nanoparticles with siRNA targeting XIAP in vivo

XIAP is often over-expressed in cancer and is an important barrier to normal apoptosis activation in cancer cells [28]. Therefore, we evaluated the *in vivo* anti-tumor effects of NP-DOX-siXIAP-Dy755 nanoparticles. We randomized H292 tumor-bearing mice into 4 experimental groups: (i) untreated, (ii) NP-DOX-Dy755 nanoparticles, (iii) NP-siXIAP-Dy755 nanoparticles and (iv) NP-DOX-siXIAP-Dy755 nanoparticles. Using near infra-red (NIR) imaging to visualize the DyLight 755 signal from the nanoconstructs, we found that nanoparticles preferentially localized to the H292 tumors over time, which was especially pronounced with DOX-incorporated nanoparticles (NP-DOX-Dy755 and NP-DOX-siXIAP-Dy755) (Fig. 6c). Tumor-bearing mice treated twice-weekly with NP-DOX-siXIAP-Dy755 were the only group to exhibit tumor-growth arrest over the 22-day treatment period (Fig. 6d, e). In contrast, control mice exhibited unchecked tumor growth, resulting in tumors approximately 6-fold larger than those in the NP-DOX-siXIAP-Dy755 group at day 22 (Fig. 6d, e). All mice tolerated repeated nanoparticle administrations as demonstrated by stable weights (Fig. 6f). After the treatment period, XIAP protein levels were significantly attenuated in tumors explanted from NP-DOX-siXIAP-Dy755 treated mice compared with controls (Fig. 6g). Furthermore, immunohistochemistry of explanted tumors revealed a significant reduction of XIAP expression in NP-DOX-siXIAP-Dy755 treated mice compared to control mice (Fig. 6h), reflecting significant *in vivo* siRNA delivery by NP-DOX-siXIAP-Dy755 particles. Both microscopic and EM examination of murine heart tissues revealed normal-appearing cardiomyocytes from all mice receiving nanoparticles (Fig. 6h, Supplemental Fig. 2), and confirmed a lack of DOX-associated cardiotoxic morphology.

4. Discussion

Nanoparticles offer a versatile platform for siRNA and drug delivery; however, inefficient transfer of nanoparticles across the cancer cell membrane may result in insufficient intracellular levels of therapeutics to render clinically significant effects. In the present study, we found that cancer cells preferentially internalize calcium phosphate nanoparticles via caveolin-mediated endocytosis and that incorporation of ultra-low non-cytotoxic amounts of doxorubicin increases the pool of free unbound caveolin-1 by disassociating eNOS-caveolin complexes. The doxorubicin-incorporated nanoparticles thereby amplified the internalization of nanoparticles delivering siRNA. This work demonstrates efficient and robust delivery of siRNA against XIAP in both *in vitro* and *in vivo* studies, resulting in marked down-regulation of XIAP and significant tumor growth arrest.

Unbound caveolin-1 participates in caveolin-mediated endocytosis; however, in the baseline state of the cancer cell, a fraction of the total intracellular caveolin-1 remains unavailable for this process and is sequestered in an inactive form as eNOS-caveolin complexes. Intracellular doxorubicin can bind avidly to the eNOS reductase domain (K_m = 5 μM), generating reactive oxygen species, and causes disassociation of the eNOS-caveolin complex to expand the intracellular pool of free caveolin-1 [27,29]. Nanoparticle endocytosis is enhanced through amplification of this doxorubicin-mediated mechanism. In our data, we observed elevation of detectable free caveolin-1 levels within 30 min after exposure to doxorubicin-incorporated nanoparticles (Figs. 3a and 4c). Such rapid changes are not due to *de novo* caveolin-1 transcriptional or translational upregulation, but are consistent with the release of pre-existing bound caveolin-1 from eNOS-caveolin complexes. This is also corroborated by unchanged caveolin-1 RNA transcript levels even 24 h after treatment with NP-DOX-siRNA-Dy550 nanoparticles in H292 cancer cells (Fig. 4a). Doxorubicin treatment in normal SAEC cells does not increase reactive oxygen species or unbound caveolin-1 levels (Fig. 4d–e), suggesting that this mechanism is sufficiently inactive in normal cells (Figs. 1d–e, 5g–j) to further enhance selective nanoparticle activity in cancer cells.

Augmented internalization of doxorubicin-incorporated nanoparticles via enhanced caveolin-mediated endocytosis also produces greater gene silencing *in vivo* relative to siRNA concentration. In one report of three patients with malignant melanoma, up to 30 mg/m^2 of systemically delivered siRNA was needed to demonstrate targeted effects [30]. In our murine model, we observed considerable *in vivo* on-target effects at a dose of 0.017 mg/m^2 siRNA, representing greater than 1000-fold difference, although such direct comparison may not be valid across species. In other *in vivo* gene silencing reports, iRGD peptide-targeted poly(-lactic-co-glycolic acid) (PLGA) NPs [8] and mesoporous silica multi-stage liposomal NPs [31] were used to deliver siRNAs against the polo-like kinase 1 (PLK1; 0.48 μg per mouse 3 times per week) and ephrin type-A receptor 2 (EphA2; 15 μg per mouse) mRNAs, respectively. With those nanoconstructs, 47% and 80% target protein reduction were correspondingly achieved. With our DOX-incorporated nanoparticles, we also observed a remarkable 80% reduction in XIAP *in vivo* from immunoblot densitometry using 5.8 μg per mouse 2 times per week (Fig. 6g). We speculate that with dosing modification, this nanoplatform can deliver even greater amounts of therapeutic siRNA since the dose of doxorubicin in our *in vivo* studies is 0.022 mg/m^2, approximately 2700-fold lower than the recommended dose for the liposomal formulation of doxorubicin.

Calcium-phosphate is currently an FDA-approved biomaterial which may therefore facilitate more rapid clinical translation as nanomedicines. In our studies, the calcium phosphate nanoparticle platform demonstrated good *in vivo* biocompatibility and natural physiologic clearance mechanisms. The early trafficking we observed of calcium phosphate NPs in the kidney and intestines is consistent with normal physiologic processing of calcium. Also, negligible nanoparticle uptake by normal cells effectively spared normal cells from both doxorubicin and siRNA exposure. No deleterious effects were seen with repeat NP dosing and cardiotoxic morphology was not seen in cardiocytes even after 22 days of exposure to DOX-incorporated NPs. Cardio-protection from doxorubicin is attributable to doxorubicin encapsulation within the nanoconstruct, which effectively limited its exposure only to cells where significant nanoparticle internalization occurs. The favorable biodistribution results observed suggest that doxorubicin-incorporated nanoparticles distribute primarily to the tumor with no appreciable accumulation in bystander organs (Fig. 6a, b), rendering a relatively tumor-specific nanoconstruct.

5. Conclusions

Translation of nanoparticle-based therapies to the clinic has been limited by inefficient transfer of nanoparticles across the cell membrane. Pegylated triple-shell calcium phosphate nanoparticles incorporating therapeutic siRNA and ultra-low levels of doxorubicin, as we describe in this report, represent a nanoparticle that preferentially localizes to tumors *in vivo*, promotes nanoparticle internalization in a compounding manner, effectively delivers therapeutic siRNAs to cause significant down-regulation of the target protein, and, in this study, significant growth arrest *in vivo*. The nanoparticle system described in this report addresses the fundamental challenge of all anti-cancer therapy, which is the ability to get sufficient therapeutic into the cancer cell while avoiding normal tissues, and provides a strategy to directly modulate the endocytotic uptake of nanoparticles, yielding potentially wide utility in both research and clinical application.

Supplementary Material

Refer to Web version on PubMed Central for supplementary material.

Acknowledgments

This research was supported by the Intramural Research Program of the US National Institutes of Health, National Cancer Institute, and Center for Cancer Research. We thank Dr. Robert Blumenthal and Professor Matthias Epple for reviewing the manuscript and providing comments and suggestions. We also thank AK Patri, JD Clogston, L Lim, P Mannan, and SH Garfield for their technical support.

References

[1]. Matsumura Y, Maeda H. A new concept for macromolecular therapeutics in cancer chemotherapy: mechanism of tumoritropic accumulation of proteins and the antitumor agent smancs. Cancer Res. 1986; 46(12 Pt 1):6387–92. [PubMed: 2946403]

[2]. Weis SM, Cheresh DA. Pathophysiological consequences of VEGF-induced vascular permeability. Nature. 2005; 437(7058):497–504. [PubMed: 16177780]

[3]. Yuan F, Dellian M, Fukumura D, Leunig M, Berk DA, Torchilin VP, et al. Vascular permeability in a human tumor xenograft: molecular size dependence and cutoff size. Cancer Res. 1995; 55(17):3752–6. [PubMed: 7641188]

[4]. Zhang Z, Xiong X, Wan J, Xiao L, Gan L, Feng Y, et al. Cellular uptake and intracellular trafficking of PEG-b-PLA polymeric micelles. Biomaterials. 2012; 33(29):7233–40. [PubMed: 22795850]

[5]. Li W, Chen L, Huang Z, Wu X, Zhang Y, Hu Q, et al. The influence of cyclodextrin modification on cellular uptake and transfection efficiency of polyplexes. Org Biomol Chem. 2011; 9(22): 7799–806. [PubMed: 21952620]

[6]. dos Santos T, Varela J, Lynch I, Salvati A, Dawson KA. Effects of transport inhibitors on the cellular uptake of carboxylated polystyrene nanoparticles in different cell lines. PLoS One. 2011; 6(9):e24438. [PubMed: 21949717]

[7]. Morelli C, Maris P, Sisci D, Perrotta E, Brunelli E, Perrotta I, et al. PEG-templated mesoporous silica nanoparticles exclusively target cancer cells. Nanoscale. 2011; 3(8):3198–207. [PubMed: 21725561]

[8]. Zhou J, Patel TR, Fu M, Bertram JP, Saltzman WM. Octa-functional PLGA nanoparticles for targeted and efficient siRNA delivery to tumors. Biomaterials. 2012; 33(2):583–91. [PubMed: 22014944]

[9]. Lu Y, Low PS. Folate-mediated delivery of macromolecular anticancer therapeutic agents. Adv Drug Deliv Rev. 2002; 54(5):675–93. [PubMed: 12204598]

[10]. Peer D, Lieberman J. Special delivery: targeted therapy with small RNAs. Gene Ther. 2011; 18(12):1127–33. [PubMed: 21490679]

[11]. Layzer JM, McCaffrey AP, Tanner AK, Huang Z, Kay MA, Sullenger BA. In vivo activity of nuclease-resistant siRNAs. RNA. 2004; 10(5):766–71. [PubMed: 15100431]

[12]. Hassani Z, Lemkine GF, Erbacher P, Palmier K, Alfama G, Giovannangeli C, et al. Lipid-mediated siRNA delivery down-regulates exogenous gene expression in the mouse brain at picomolar levels. J Gene Med. 2005; 7(2):198–207. [PubMed: 15515135]

[13]. Landen CN Jr, Chavez-Reyes A, Bucana C, Schmandt R, Deavers MT, Lopez-Berestein G, et al. Therapeutic EphA2 gene targeting in vivo using neutral liposomal small interfering RNA delivery. Cancer Res. 2005; 65(15):6910–8. [PubMed: 16061675]

[14]. Takeshita F, Minakuchi Y, Nagahara S, Honma K, Sasaki H, Hirai K, et al. Efficient delivery of small interfering RNA to bone-metastatic tumors by using atelocollagen in vivo. Proc Natl Acad Sci U S A. 2005; 102(34):12177–82. [PubMed: 16091473]

[15]. Song E, Zhu P, Lee SK, Chowdhury D, Kussman S, Dykxhoorn DM, et al. Antibody mediated in vivo delivery of small interfering RNAs via cell-surface receptors. Nat Biotechnol. 2005; 23(6): 709–17. [PubMed: 15908939]

[16]. Medarova Z, Pham W, Farrar C, Petkova V, Moore A. In vivo imaging of siRNA delivery and silencing in tumors. Nat Med. 2007; 13(3):372–7. [PubMed: 17322898]

[17]. Reich SJ, Fosnot J, Kuroki A, Tang W, Yang X, Maguire AM, et al. Small interfering RNA (siRNA) targeting VEGF effectively inhibits ocular neovascularization in a mouse model. Mol Vis. 2003; 9:210–6. [PubMed: 12789138]

[18]. Sugimura K, Takebayashi S, Taguchi H, Takeda S, Okumura K. PARP-1 ensures regulation of replication fork progression by homologous recombination on damaged DNA. J Cell Biol. 2008; 183(7):1203–12. [PubMed: 19103807]

[19]. Zhang X, Chen ZG, Choe MS, Lin Y, Sun SY, Wieand HS, et al. Tumor growth inhibition by simultaneously blocking epidermal growth factor receptor and cyclooxygenase-2 in a xenograft model. Clin Cancer Res. 2005; 11(17):6261–9. [PubMed: 16144930]

[20]. Li SD, Chen YC, Hackett MJ, Huang L. Tumor-targeted delivery of siRNA by self-assembled nanoparticles. Mol Ther. 2008; 16(1):163–9. [PubMed: 17923843]

[21]. Zhang X, Kovtun A, Mendoza-Palomares C, Oulad-Abdelghani M, Fioretti F, Rinckenbach S, et al. SiRNA-loaded multi-shell nanoparticles incorporated into a multilayered film as a reservoir for gene silencing. Biomaterials. 2010; 31(23):6013–8. [PubMed: 20488536]

[22]. Sokolova VV, Radtke I, Heumann R, Epple M. Effective transfection of cells with multi-shell calcium phosphate-DNA nanoparticles. Biomaterials. 2006; 27(16):3147–53. [PubMed: 16469375]

[23]. Tomayko MM, Reynolds CP. Determination of subcutaneous tumor size in athymic (nude) mice. Cancer Chemother Pharmacol. 1989; 24(3):148–54. [PubMed: 2544306]

[24]. Olton DY, Close JM, Sfeir CS, Kumta PN. Intracellular trafficking pathways involved in the gene transfer of nano-structured calcium phosphate-DNA particles. Biomaterials. 2011; 32(30): 7662–70. [PubMed: 21774979]

[25]. Luhmann T, Rimann M, Bittermann AG, Hall H. Cellular uptake and intracellular pathways of PLL-g-PEG-DNA nanoparticles. Bioconjug Chem. 2008; 19(9):1907–16. [PubMed: 18717536]

[26]. Belanger MM, Roussel E, Couet J. Up-regulation of caveolin expression by cytotoxic agents in drug-sensitive cancer cells. Anticancer Drugs. 2003; 14(4):281–7. [PubMed: 12679732]

[27]. Feron O, Saldana F, Michel JB, Michel T. The endothelial nitric-oxide synthasecaveolin regulatory cycle. J Biol Chem. 1998; 273(6):3125–8. [PubMed: 9452418]

[28]. Xie Y, Tobin LA, Camps J, Wangsa D, Yang J, Rao M, et al. MicroRNA-24 regulates XIAP to reduce the apoptosis threshold in cancer cells. Oncogene. 2012 http://dx.doi.org/10.1038/onc.2012.258 [Epub ahead of print].

[29]. Vasquez-Vivar J, Martasek P, Hogg N, Masters BS, Pritchard KA Jr, Kalyanaraman B. Endothelial nitric oxide synthase-dependent superoxide generation from adriamycin. Biochemistry. 1997; 36(38):11293–7. [PubMed: 9333325]

[30]. Davis ME, Zuckerman JE, Choi CH, Seligson D, Tolcher A, Alabi CA, et al. Evidence of RNAi in humans from systemically administered siRNA via targeted nanoparticles. Nature. 2010; 464(7291):1067–70. [PubMed: 20305636]

[31]. Tanaka T, Mangala LS, Vivas-Mejia PE, Nieves-Alicea R, Mann AP, Mora E, et al. Sustained small interfering RNA delivery by mesoporous silicon particles. Cancer Res. 2010; 70(9):3687–96. [PubMed: 20430760]

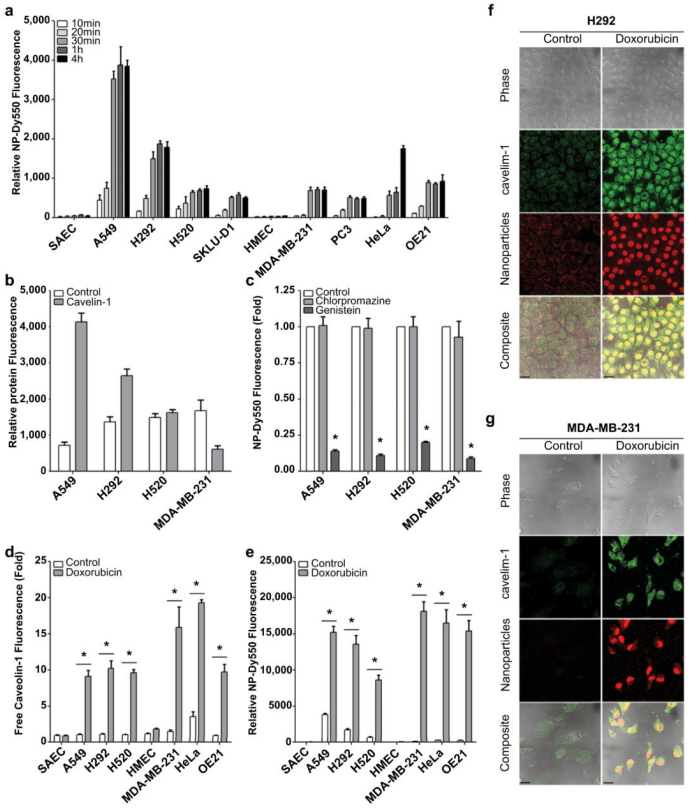

Fig. 1.

Doxorubicin enhances caveolin-mediated endocytosis in a panel of cancer cells. (a) Relative fluorescence of pegylated triple-shell calcium phosphate nanoparticle labeled with DyLight 550 (NP-Dy550) in NSCLC (A549, H292, H520, SKLU-1), breast (MDA-MB-231), prostate (PC3), cervical (HeLa) and esophageal (OE21) cancer cells and normal epithelial cells (SAEC and HMEC) after up to 4 h incubation at 37 °C. Data are means ± s.e.m. ($n \geq$ 25 cells per time point). (b) Relative clathrin and free unbound caveolin-1 protein signal per cell. Bars represent mean ± s.e.m. ($n \geq 25$ cells) as measured by fluorescence confocal microscopy. (c) Inhibition of caveolin-mediated endocytosis by genistein (GEN; 400 μM) reduces nanoparticle accumulation in cancer cells; however, inhibition of clathrin-mediated endocytosis by chlorpromazine (CPZ; 10 μg/mL) does not significantly alter NP cell-entry rates. Bars represent mean NP-Dy550 fluorescence per cell after a 1 h pre-treatment with CPZ or GEN inhibitor followed by NP-Dy550 incubation for 0.5 h. Data are means ± s.e.m. ($n \geq 25$ cells, $^*p < 0.05$ for treatment compared to control using Student's t test). (d–e) Pre-treatment with doxorubicin (DOX; 50 nM) followed by a 4 h incubation with NP-Dy550 at 37 °C increases unbound caveolin-1 levels in cancer cells (d) and results in enhanced nanoparticle uptake compared to controls (e). Bars represent means ± s.e.m. ($n \geq 25$ cells, $^*p < 0.05$ for a 2 h pre-treatment with doxorubicin compared to control using Student's t test). (f–g) Representative confocal micrographs of doxorubicin pre-treated H292 (f) and MDA-MB-231 (g) cancer cells 4 h after administration of NP-Dy550. Scale bars, 20 μm.

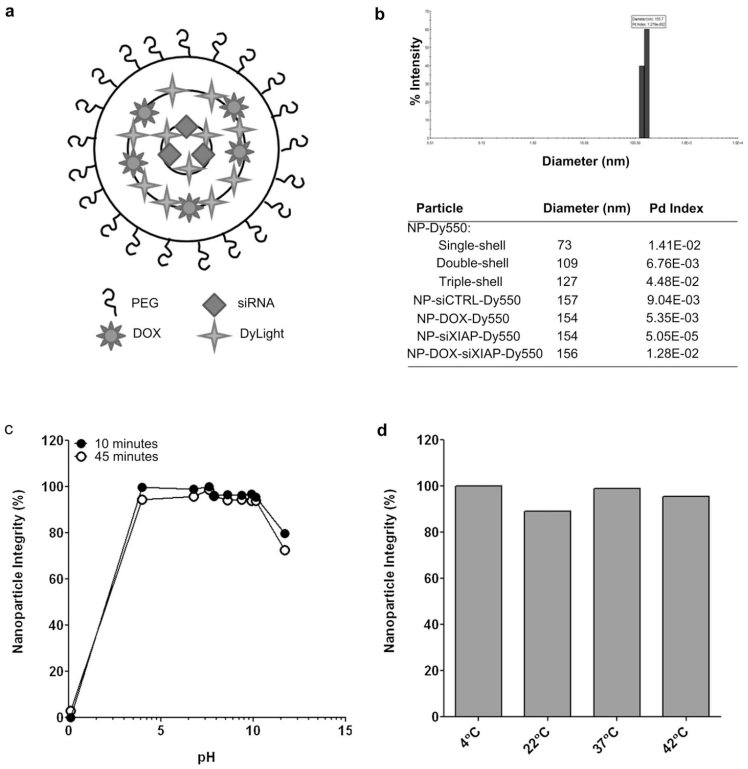

Particle	Diameter (nm)	Pd Index
NP-Dy550:		
Single-shell	73	1.41E-02
Double-shell	109	6.76E-03
Triple-shell	127	4.48E-02
NP-siCTRL-Dy550	157	9.04E-03
NP-DOX-Dy550	154	5.35E-03
NP-siXIAP-Dy550	154	5.05E-05
NP-DOX-siXIAP-Dy550	156	1.28E-02

Fig. 2.

Characterization of doxorubicin and siRNA-incorporated nanoparticles. (a) Composition of pegylated triple-shell calcium phosphate nanoparticles with DOX in the secondary (middle) shell and siRNA in the primary (inner) shell. DyLight 550 (Dy550) or 755 (Dy755) fluorescent dyes were incorporated in the primary and secondary shells. (b) Particle diameter and polydispersity (Pd) index of single-, double-, and triple-shell nanoparticles incorporating DyLight 550, DOX, and/or siRNA (negative control siRNA, siCTRL; siRNA against XIAP, siXIAP) as measured by dynamic light scattering. Representative graph of particle diameter and polydispersity of NP-DOX-siXIAP-Dy550 based on intensity by dynamic light scattering. (c–d) Integrity of NP-DOX-siXIAP-Dy550 after up to a 45 min exposure to a series of pH values (0.1–10.1) (c) or temperatures (4–42 °C) (d).

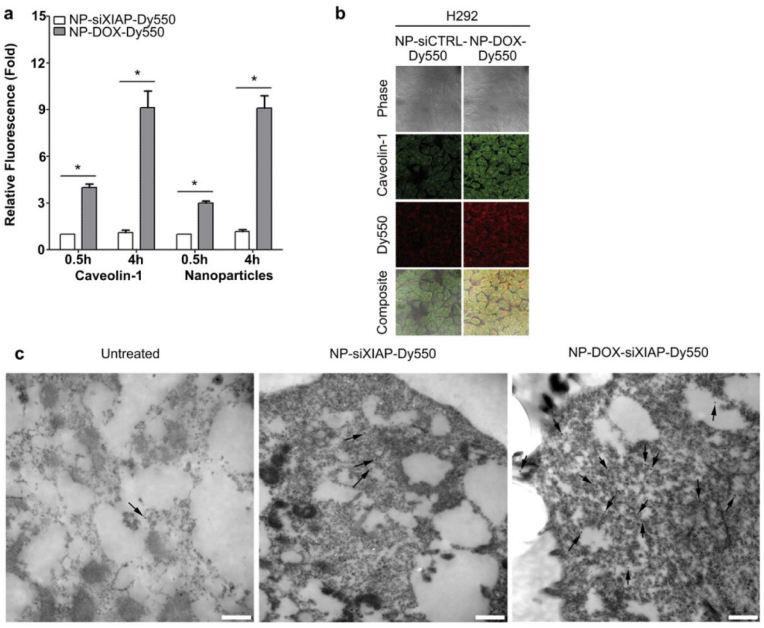

Fig. 3.

Doxorubicin-incorporated triple-shell nanoparticles enhance nanoparticle uptake into cancer cells *in vitro*. (a–b) Unbound caveolin-1 levels and nanoparticle uptake are enhanced in H292 cells following a 0.5 or 4 h incubation with doxorubicin-incorporated nanoparticles (NP-DOX-Dy550). Bars represent means ± s.e.m. ($n \geq 25$ cells, $^*p < 0.05$ for NP-DOX-Dy550 compared to NP-siCTRL-Dy550 using Student's *t* test). (b) Representative confocal micrographs of H292 cells after a 4 h treatment with NP-siCTRL-Dy550 or NP-DOX-Dy550 and corresponding free caveolin-1 expression. (c) Representative immuno-EM photomicrographs of unbound caveolin-1 levels in H292 cells following a 4 h treatment with NP-siXIAP-Dy550 or NP-DOX-siXIAP-Dy550. 15 nm gold-conjugated secondary antibodies, black arrows. Scale bars, 500 nm.

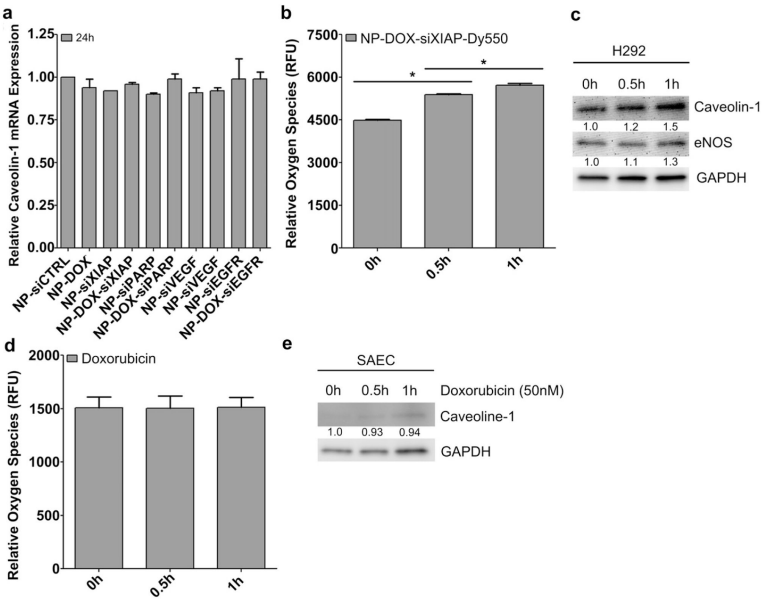

Fig. 4.

Intracellular doxorubicin causes disassociation of eNOS-caveolin complexes in cancer cells to increase the pool of unbound caveolin-1. (a) Caveolin-1 mRNA expression is unchanged in H292 cells after a 24 h incubation with doxorubicin-incorporated nanoparticles. Bars represent means ± s.e.m. ($n = 3$). (b) Relative reactive oxygen species (ROS) in H292 cells treated for up to 1 h with NP-DOX-siXIAP-Dy550. Significant generation of ROS occurs at early time points after treatment with nanoparticles. Bars represent means ± s.e.m. ($n = 3$, $^*p < 0.05$ using Student's t test). (c) Representative western blot for free caveolin-1 and eNOS in H292 cells following a 0.5 or 1 h incubation with NP-DOX-siXIAP-Dy550 showing increases in free caveolin-1 and eNOS. (d) ROS levels remain unchanged in normal SAEC cells following doxorubicin (50 nM) treatment. Bars represent means ± s.e.m. ($n = 3$). (e) Representative western blot for unbound caveolin-1 in SAEC cells following a 0.5 or 1 h incubation with doxorubicin (50 nM).

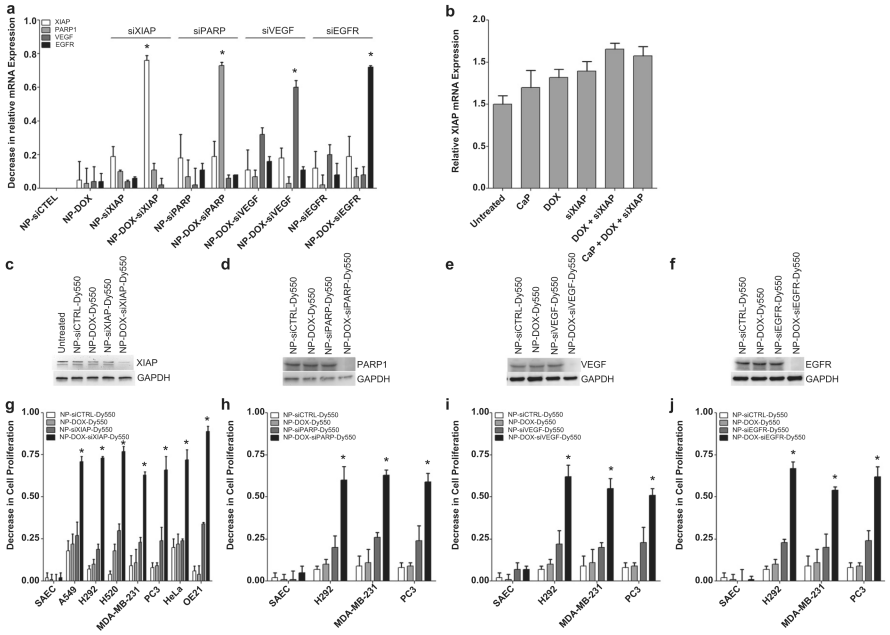

Fig. 5.

Doxorubicin-incorporated nanoparticles enhance siRNA delivery and target-specific knock-down in cancer cells. (a) A decrease in relative mRNA expression of XIAP, PARP, VEGF, and EGFR in H292 cells following a 24 h treatment with corresponding nanoparticles. Bars represent means ± s.e.m. ($n = 3$ independent experiments, $*p < 0.05$ compared to NP-siCTRL-Dy550 treated cells using Student's t test). (b) H292 cells treated for 24 h with the un-assembled components of NP-DOX-siXIAP-Dy550 (calcium phosphate (CaP), DOX, and/or siXIAP) do not decrease relative XIAP mRNA levels compared to untreated cells. Bars represent means ± s.e.m. ($n = 3$). (c–j) 48 h treatment with NP-DOX-siRNA-Dy550 nanoparticles targeting XIAP (c, g), PARP1 (d, h), VEGF (e, i) or EGFR (f, j) results in significant knock-down of specific target proteins (c–f) and decreased cell viabilities (gej) in a panel of cancer cells. Bars represent means ± s.e.m. ($n = 3$ independent experiments, $*p < 0.05$ for NP-DOX-siRNA-Dy550 compared to NP-siCTRL-Dy550, NP-DOX-Dy550, or NP-siRNA-Dy550 using Student's t test).

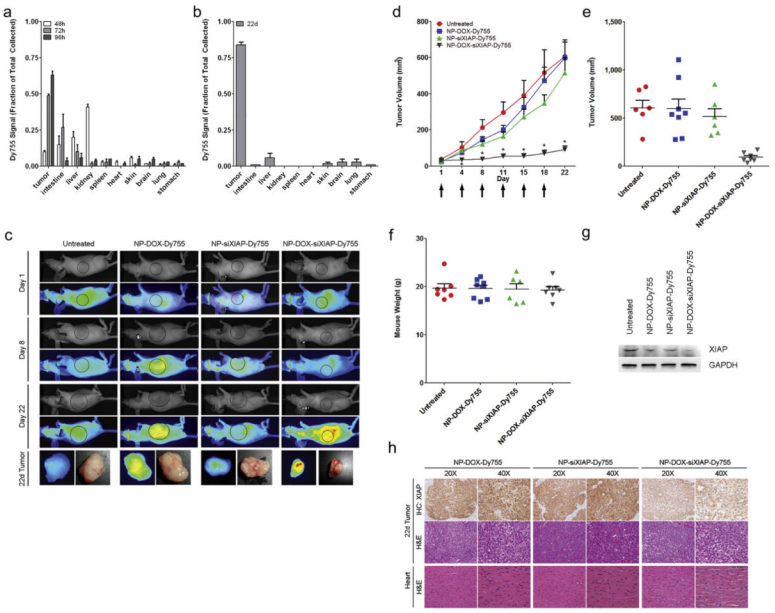

Fig. 6.

NP-DOX-siXIAP-Dy755 administered intravenously accumulates in H292 tumors in vivo to cause tumor growth arrest. (a, b) NP-DOX-siXIAP-Dy755 anatomic biodistribution of a single intravenous dose at 48, 72, and 96 h (a) and at day 22 after twice-weekly nanoparticle injections (b). Data are means ± s.e.m. ($n = 3$ mice for each group per time point). (c) H292 tumor-bearing mice (right flank) were serially imaged for NIR fluorescence (Dy755) from day 1 (prior to nanoparticle injection) up to day 22 after completion of three cycles of twice-weekly injections of NP-DOX-Dy755 (8 μg DOX/dose), NP-siXIAP-Dy755 (5.8 μg siRNA/dose) or NP-DOX-siXIAP-Dy755 (8 μg DOX and 5.8 μg siRNA/dose). White light and near-infrared fluorescence shown as pseudo-color heat-map images of representative mice and explanted tumors at day 22. (d) Target-specific tumor growth inhibition with twice-weekly intravenous injection (denoted by arrows) of NP-DOX-siXIAP-Dy755 nanoparticles. Data are means ± s.e.m. ($n \geq 7$ mice in each group, $^*p < 0.05$ for NP-DOX-siXIAP-Dy755 treatment compared to the other control groups using a Krushkal–Wallis test with post-testing). (e–f) Distribution of mouse tumor volumes (e) and mouse weights (f) among experimental groups at day 22. (g) Representative western blot of XIAP protein levels in H292 tumors excised from mice after 22 days of nanoparticle treatment. Tumors of NP-DOX-siXIAP-Dy755 treated mice demonstrate a significant decrease in XIAP protein levels compared to controls. (h) Immunohistochemistry (IHC) for XIAP and H&E of explanted tumors from NP-DOX-Dy755, NP-siXIAP-Dy755, and NP-DOX-siXIAP-Dy755 treated mice after 22 days. H&E of heart tissues are also shown, demonstrating no histologic evidence of myocardial abnormalities.